KINETICS OF DOMAIN FORMATION BY SICKLE HEMOGLOBIN POLYMERS

SOUMEN BASAK, FRANK A. FERRONE, AND JIN TONG WANG
Department of Physics and Atmospheric Science, Drexel University, Philadelphia, Pennsylvania 19104

ABSTRACT We have monitored the growth of domains of sickle hemoglobin polymers by using temporally and spatially resolved light scattering and birefringence measured pseudosimultaneously on a 50-μm square area. Polymerization was induced and indefinitely maintained by photolysis of the carbonmonoxy derivative using an argon ion laser. Intensity of scattering and birefringence (measured as intensity transmitted through crossed polarizers) were measured using a silicon-intensified target vidicon interfaced to a computer. Polymer concentration, as inferred by light scattering, grew with primarily circular symmetry, with ~20% of the signal initially in a twofold symmetric pattern. In time the circular symmetry increased. A distinct decrease in the scattering signal developed which spread outward from the center of the domain. Birefringence lagged the scattering and initially grew in a twofold pattern, with the formation of a characteristic Maltese cross only appearing much later, and well after the scattering signal had peaked. Radial profiles of the domain scattering and birefringence were both approximately gaussian. We successfully modeled the decrease in scattering by fitting the profiles to a large gaussian from which a second smaller gaussian was subtracted. This second gaussian had the width of the birefringence gaussian. The width of the birefringence gaussian grew linearly in time, while the width of the scattering gaussian showed a notable acceleration. We conclude that domains form primarily as disordered arrays which align at later times. We explain the above observations, including the shape of the birefringence progress curves, as the result of an alignment transition which is solely due to a redistribution of monomers from short to long, and from entangled to radial, polymers. We present a theoretical justification for this process in an appendix. In a separate paper (Zhou, H. X., and F. A. Ferrone, manuscript submitted for publication) we show that the gaussian shapes and acceleration of the width naturally arise from a generalization of the double nucleation mechanism for sickle hemoglobin gelation (Ferrone, F. A., J. Hofrichter, H. Sunshine, and W. A. Eaton. 1980. *Biophys. J.* 32:361–377; Ferrone, F.A., J. Hofrichter, and W.A. Eaton. 1985. *J. Mol. Biol.* 183:611–631).

INTRODUCTION

Upon deoxygenation, sickle cell hemoglobin molecules in concentrated solutions assemble into 14 stranded fibers (Dykes et al., 1978) which form a viscous gel. It has long been observed that the fibers themselves are typically found in arrays called domains. These domains are recognized as a Maltese cross seen when the gel is viewed between crossed polarizers (Hofrichter et al., 1976; White and Heagan, 1970). Rotation of the cross as the polarizer pair rotates implies that the gel is composed of radially aligned fibers. A similar conclusion is reached using more sophisticated model building from polarized images (Beach et al., 1988). White and Heagan (1970) directly observed radially oriented fibers in a series of electron micrographs at a variety of levels of magnification. By linear dichroism measurements, Hofrichter (1986) has found that these radial arrays (spherulites) are of rather uniform density and show no angular dependence. In regions far from the domain center, the fibers show a high degree of alignment (Sunshine et al, 1982). The speed of gelation is found to correlate with the number of domains in a given sample (Ferrone et al, 1980). Recently Mickols et al. (1985, 1988) have begun the collection of systematic information about the equilibrium distribution of the domains, their sizes, and structures. However, there is no information about the kinetics of the formation of domains.

A significant relationship between domains and the kinetics of gelation was first established in measurements of the stochastics of gelation in small sample volumes (Ferrone et al., 1980, 1985*a*; Hofrichter, 1986). In those experiments, a single domain of polymers was found to form with a rate exhibiting stochastic fluctuations. Once initiated however, the subsequent growth of the domain showed fully reproducible deterministic behavior. This was a pivotal observation in formulating a double nucleation mechanism, suggesting as it did that a single molecular event could proliferate into an array of many polymers. The double nucleation mechanism explained this behavior by the postulate that new polymers could nucleate on the surface of preexisting polymers. That mechanism success-

Dr. Basak's present address is Saha Institute of Nuclear Physics, Calcutta, India. Dr. Wang's present address is Lincoln University, Lincoln University, PA 19352.

fully provided a kinetic framework which described the polymerization reaction over six decades of rates, in the concentration range 20–40 g/dl, and the temperature range 5–50°C. (Ferrone et al, 1985*b*).

With the advent of the double nucleation mechanism the manner in which essentially linear polymers are transformed into radial arrays becomes more than a curiosity. A domain is thus seen as the evolution of a polymer network after a single homogeneous nucleation event. The heterogeneous pathway for polymer formation must provide at least the initial geometry for proliferation of polymers into a domain, and conceivably could determine the resultant domain geometry in its entirety.

We have begun studies on the kinetics of domain formation using laser photolysis to initiate the reaction. We employ a new technique in which the spatial extent of the domain is resolved in time. By observing both light scattering and birefringence we measure the total polymer mass as well as the aligned component of polymers. Because the technique has not been fully described, and because it is integral to the measurements, it is described in some detail here.

In this report only a single concentration has been studied. Our initial goals are simple: to characterize the symmetry of the growing aggregate, to compare alignment and total polymer content, and to measure the rate of domain expansion for comparison with the double nucleation mechanism.

MATERIALS AND METHODS

Samples of COHbS in 0.15 M phosphate buffer, pH 7.35, with 60 mM sodium dithionite, were prepared and characterized as described elsewhere (Ferrone et al., 1985*a*). Samples were stored in sealed quartz EPR tubes (Wilmad) under a water saturated CO atmosphere in the cold. The sample concentration for the experiments reported here was 0.313 g/cm^3. Optical experiments were carried out on a slide made by sealing a thin layer (4–6 μm) of COHbS between two coverslips using Kerr sticky wax (Emeryville, CA), and attaching the slide to a Cambion thermoelectric stage equipped with homemade controller. To permit operation below the dew point, a nitrogen flow system keeps the slide in a dry environment. Stage temperatures used in these experiments ranged between 5 and 20°C.

The instrument on which the kinetics were measured is a horizontal microspectrophotometer constructed on an optical table (Newport Corp., Fountain Valley, CA) with isolation mounts. A schematic of the apparatus is shown in Fig. 1. The principal path through the optical system originates in a 150-Watt xenon arc lamp and Oriel f/5.3 monochromator, passes through a Koehler illumination system, through 10× long-working distance objectives (E. Leitz, Rockleigh, NJ) and a 10× eyepeice, and is detected by a silicon intensified target vidicon. A beam splitter directs a similar image to a TV monitor. For reference measurements, part of the monochromator beam is deflected into a photomultiplier tube.

The entire experiment is controlled by an LSI 11/73 computer with hard disk. A stepper motor, interfaced to the computer, controls the monochromator. The computer also directs the opening of the mechanical shutters and the switching of filters as described below. The reference photomultiplier signal is read by an A/D converter, as is the photodiode which monitors laser power. Vidicon data is collected by a PAR 1216 controller and is processed by the computer and stored on hard disk. Long term storage is by means of 8-inch floppy disks.

Laser photolysis of the CO derivative was used to create and indefinitely maintain a small volume of deoxy HbS (Ferrone et al., 1980, 1985*a*, Coletta et al., 1982; Hofrichter 1987; Mozzarelli et al., 1987). An argon ion laser (model 164, Spectra-Physics Inc., Mountain View, CA) operated multiline, provides the 514-nm photolysis beam, which is also the source beam for light scattering measurements, and the 488-nm birefringence source beam. The laser output beams are interrupted by a computer-interfaced mechanical shutter and dispersed by a prism. The photolysis/scattering beam is incident at ~45° on the sample and focussed by a simple lens of focal length 15 cm; a piece of this beam is picked off by a glass wedge and monitored by a model 815 (Newport Corp., Fountain Valley, CA) photodiode calibrated against a Scientech 362 power meter (model 362, Scientech Inc., Boulder, CO). For birefringence measurements, the 488-nm beam is directed through the field diaphragm in place of the arc lamp and monochromator. The 488-nm beam was enlarged by a simple lens so that only a portion of it was imaged onto the sample. The polarization axis of this birefringence beam is rotated by polarizer P_1, then set by P_2 to extinguish against P_3 in front of the vidicon. Polarizer P_3 also reduces the scattered intensity, thereby keeping the vidicon intensity within calibration (see below). Spatially resolved, pseudosimultaneous light scattering and birefringence are used to monitor the growth of the domains, with an externally triggered filter changer (ETFC) with narrow band interference filters employed to select the 514- or 488-nm beam for

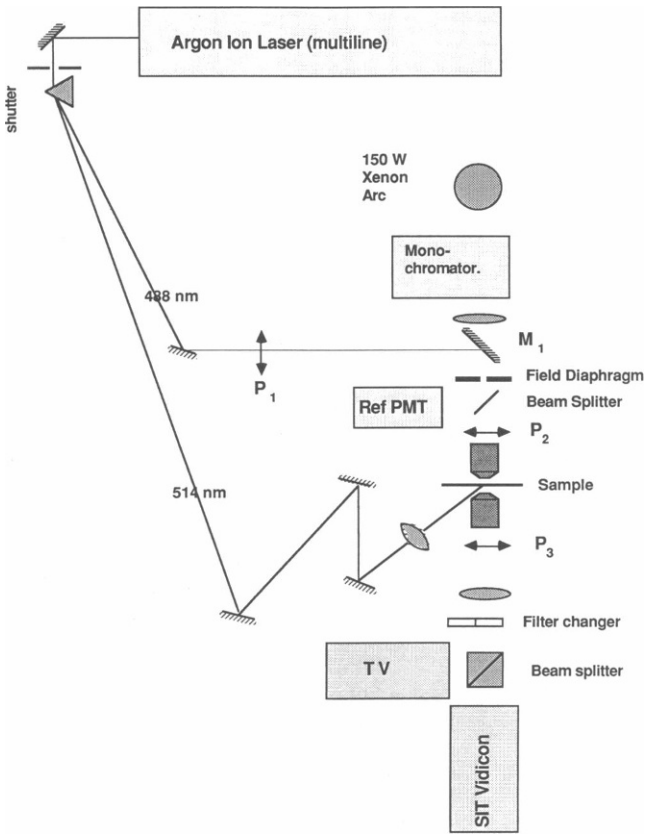

FIGURE 1 Schematic of the apparatus. As shown the instrument is configured for collecting pseudosimultaneous scattering and birefringence data. The filter changer alternately inserts a narrow band 514 or 488-nm filter in the beam. P_1, P_2, and P_3 are polarizers, arranged so that P_3 transmits ~10% of the scattered beam (to prevent the vidicon from operating in the saturation region of its intensity response curve) whereas P_2 is crossed with respect to P_3. The presence of P_1 allows for adjustment of the intensity in the 488-nm beam impinging on the sample. For absorbance measurements, the mirror M_1 is removed and the arc lamp and monochromator provide the light source. In that case, the filter changer is also removed.

the detector (Basak and Ferrone, 1988*a*). For desaturation or spectral measurements, the ETFC is replaced by a simple filter.

Detector Calibration

The SIT vidicon is controlled by a Princeton Applied Research (Princeton, NJ) 1216 OMA controller interfaced to an LSI 11/73 computer. The vidicon itself has a face array of 512 × 512 pixels. 50 tracks of 4-pixel height were scanned. Before each scan the vidicon was cleared by two prep frames. Each track scan included 200 channels (i.e., 1 pixel wide × 4 pixels high), but channels were averaged in a macro routine as groups of four. Reading time on each channel was 40 μs, and 15 additional channels were collected on each track to account for charge leakage. Thus a data array was collected on a 50 × 50 grid. After magnification of the optical system is included, the system is found to dissect a square area of the sample 50 μm on a side into 2,500 elements. (In a few experiments, we employed 3 track/3 channel averaging, so that the 50 × 50 grid represented a sample section measuring 37.5 μm on a side.)

The response on the SIT detector is both nonlinear and nonuniform, thus requiring calibration of each element of the entire grid. The vidicon gain was calibrated by fitting the relative intensity, I_0, reduced by calibrated neutral density filters (absorbance OD_j) to a third order polynomial in the counts detected per element, $N(x, y)$, i.e.,

$$I(x, y) = I_0(x, y)\ 10^{-OD_j} = c_1(x, y)\ N(x, y) + c_2(x, y)\ N^2(x, y) + c_3(x, y)\ N^3(x, y) \quad (1)$$

(Basak and Ferrone, 1988*b*). The formulation of I as a polynomial in N was motivated by the desire to retain computational speed, which would not have been possible had the function been constructed with N as a polynomial in I, requiring a nonlinear inversion for each of 2,500 pixels each time a calibrated intensity was required. The formulation was normalized so that a single count at the vidicon gave an intensity of unity. This procedure worked quite well, with most deviations <5%. For intensities less than ~4% of the maximum, the quality of the fit worsened to ~25% error. This is indicative of the fact that a more complex function is required for full range accuracy. Because the bulk of the data is collected with high intensities, the speed and flexibility of this polynomial was deemed adequate compensation for the small inaccuracy. In particular, the most sensitive measurements involve measuring optical density changes, all of which involve high and well-calibrated intensities.

Beam Profile Determination

Before data collection on each experiment, a profile of the laser beam was obtained by measuring the scattering from a 10% aqueous suspension of 0.173 μm diameter latex spheres. 20 frames were averaged and fit with a skewed gaussian. The exact form of gaussian arises because the laser does not lie in the same plane as the optical path and because the sample plane intersects the beam cone at an angle. It should be noted, however, that any empirical function would suffice, so long as the beam shape is reproduced accurately. The intensity in the plane which intersects the expanding gaussian is given in rotated coordinates u, v by

$$I = I_0 \exp(-u^2/\sigma_u^2) \exp(-v^2/\sigma_v^2), \quad (2)$$

where

$$\sigma_u = a_u + b_u u \quad \text{and} \quad \sigma_v = a_v + b_v v, \quad (3)$$

and the coordinates u and v represent a simple rotation of the sample coordinates x and y via the transformation

$$u = (x - x_0)\cos\theta + (y - y_0)\sin\theta \quad (4a)$$

$$\text{and } v = (y - y_0)\cos\theta - (x - x_0)\sin\theta. \quad (4b)$$

Thus there are eight parameters to describe the beam: I_0, x_0, y_0, a_u, b_u, a_v, b_v, and θ. Scattering data from the latex solution was fit by a standard nonlinear curve fitting algorithm using these eight parameters (Bevington, 1969).

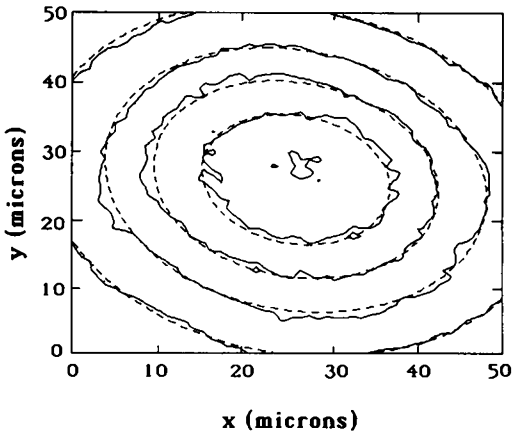

FIGURE 2 Comparison of a typical measurement of the laser beam intensity profile and its fit to Eq. 2–4 of the text. Intensity contours for the laser scattering from a 10% aqueous suspension of 0.173 μm diameter latex spheres, after smoothing, are drawn as solid curves. The contours for the fit of Eqs. 2–4 are drawn as dotted lines. Both sets of contours represent 20% intervals on the gaussian profile, whose center is taken to be that of the rectangle. The best-fit parameters for this profile are: a_u = 23.3 μm, b_u = 0.0017, a_v = 19.2 μm, b_v = −0.0165, θ = −23.3 degrees.

Fig. 2 shows intensity contours for scattering from a typical beam, together with the fit of such a gaussian. Contours are drawn at 20% intervals of the fit, and the corresponding data line contours are also shown. As can be seen, the fit matches the data very well. The average deviation for the 2,500 points in nine different experiments was 5.24 ± 0.78%. Average radii (parameters a_u and a_v) were 24.6 ± 1.6 μm (horizontal) and 20.0 ± 1.2 μm (vertical). The errors in the above parameters are the difference between measurements for different experiments (rather than fitting error) and are indicative of the reproducibility of the optical system.

Laser Heating

In previous applications of this photolysis technique (Ferrone et al., 1980, 1985*a*; Coletta et al., 1982; Hofrichter 1986; Mozzarelli et al., 1987), small beam sizes kept the laser-induced temperature rise low and fairly uniform. However, decreasing the spot size to control the laser heating reduces the area available for studying domain fomration. The beam size used here represents a compromise between these goals, at the cost of some uniformity in the heating obtained. Because domains may be nucleated in various parts of the sample, not only the maximum temperature rise but also the spatial variation of the temperature rise must be known.

Using Liebmann's method (Gerald, 1978) we numerically solved the steady-state heat conduction equation (Laplace's equation). A numerical solution is required because of the complexity of the boundary conditions. For simplicity, the geometry of this experiment was modeled as heat evolved by a simple guassian of revolution in an aqueous (protein) layer in contact with finite glass slabs. Thus the temperature rise was calculated given the input laser power, beam size, and sample thickness and optical density.

The temperature rise was found to be similar in shape to a gaussian (though not exact), and somewhat wider than the laser beam. For purposes of comparison, we fit the central part of the temperature rise by a gaussian and obtained a gaussian width of 37.2 μm vs. 22.3 μm laser radius. This implies that there will be smaller thermal gradients than if the temperature rise mirrored the variation of the laser across the sample (e.g., Fig. 2). The peak temperature rise was calculated to be 2.2°C per

kW/cm² of laser intensity incident on the sample. Because the maximum laser power used was 2.6 kW/cm², the maximum temperature rise here was 5.9°C, with most experiments using <1.5 kW/cm² (for a 3.3°C rise) and therefore having a gradient across the observed area one degree or less.

To test the adequacy of this calculation, control experiments were performed with a 1 M solution of cresol red dye in Tris buffer, pH 8. The temperature-induced change in the buffer is then observed by changes in absorption of the indicator dye at 570 nm. An interference filter at that wavelength was used to reject dye fluorescence. By observing the fluorescence alone the laser could be appropriately centered, and its focus in the sample plane confirmed. Included in the calculation for this control experiment is a decay of the energy absorbed with distance into the sample, because the cresol solution was not optically thin. The measured temperature rise was 6.1°C which agrees satisfactorily with a calculated temperature increase of 7.6°C. A further test is afforded by comparing the calculation with the extensive data set of Ferrone et al. (1985*a*) as listed in Table III there. Those experiments employed optically thin samples and a smaller diameter laser beam. The calculations reproduced the measured heating coefficients within 20% there as well.

Absorption and Desaturation Measurements

Sample absorption spectra were measured using the arc lamp and monochromator. The vidicon scan was configured to read the average over the entire 2,500 grid elements of each wavelength, so as to collect a single spectrum. The peak optical density of the Soret band (419 nm) ranged between 1.0 and 2.0. This spectrum was generally well fit by a standard CO spectrum measured on macroscopic samples (Ferrone, unpublished results), with occasional deviations occurring at the peak because the low count region had the greatest calibration error. The absorbance at 419 nm was then measured for each element of the grid to guarantee the homogeneity of the region selected. In all cases 95% or more of the grid elements were within ±0.1 OD of the mean, and no notable gradients were visible.

To account for the spatial variation in source brightness of the light scattering beam (514 nm laser line), it was necessary to locate the beam center on the $COHb_S$ sample. To do this, as well as to monitor desaturation, the optical density profile of the $COHb_S$ sample at 432 nm was collected immediately after photolysis was begun, and the center of the photolyzed spot was taken to be the beam center in all subsequent analysis. A problem arises because the readout of the vidicon is not instantaneous. A scan begun at the lower left will finish at the upper right grid element some 2.44 s later. Desaturation proceeds rapidly enough that this creates image distortion. This problem was rectified here by performing repeat experiments, one with a scan starting from the bottom of the vidicon face, the other with a scan begun at the top, and averaging the desauturation profiles determined in this fashion. (The left-to-right time discrepancy is not as great. Horizontally adjacent grid elements are separated by only 0.16 ms but vertically adjacent elements are separated by 47.24 ms.) Fig. 3 *A* shows such an up-down average. The picture corresponds to an average time after initiation (shutter opening) of 1.2 s.

Fig 3 also shows the evolution of the desaturation spot. The pattern enlarges due to the diffusion of free CO away from the photolyzed volume, allowing a given power density to create a greater degree of photolysis. Note the difference in the first frame, which is not averaged, compared with the up-down average in Fig. 3 *A*. The measured photolysis levels are acceptably close to those predicted by absorption spectra taken on a sample before use. Power densities at the sample ranged between 0.5 and 1.4 kW/cm². To limit the heating artifact, the power densities used here are deliberately lower than used previously (Ferrone at al., 1985*a*) and may account for a small increase in apparent delay time. At the first measured frame desaturation was generally >95%, and in all cases it was ascertained that the change in absorbance due to photolysis has saturated, so that photolysis was deemed complete.

The change in absorbance due to photolysis, $\Delta A(x, y)$, determined by the up-down average, allows the beam center to be determined. The center determined by scattering from latex will not in general be the same beam center due to small differences in the sample thickness, slide thickness and curvature, etc. The other beam parameters (e.g., width) will not change. The center corrdinates x_1 and y_1 are then calculated according to

$$x_1 = \Sigma\, x\Delta A(x, y)/\, \Sigma\, \Delta A(x, y) \qquad (5a)$$

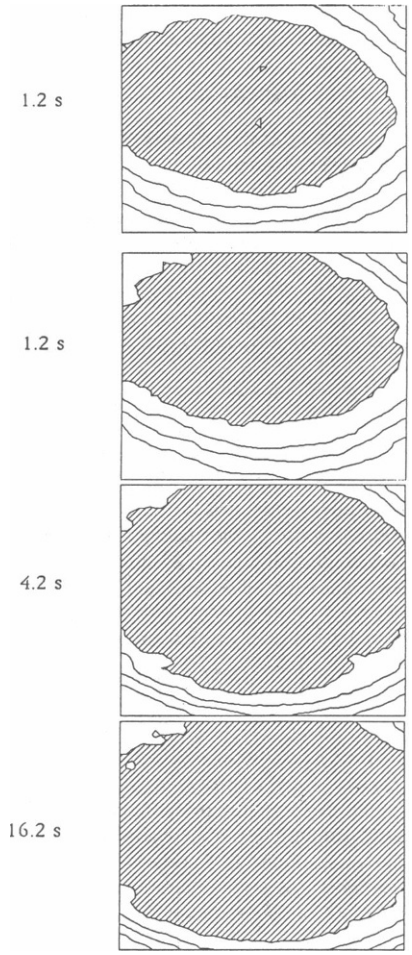

FIGURE 3 Evolution of spatial profile of photolysis produced by the laser beam, measured by monitoring the increase of absorbance at 432 nm due to the conversion of carbonmonoxy-HbS to deoxygenated HbS. The contours represent 20% intervals on the profiles, the central shaded region in each panel thus defining the region with photolysis levels of 80% and above. The dimensions of each frame are 50 × 50 μm. (The contour program has created some apparent triangles which arise from noise in the contour map.) (*a*) Profile obtained by averaging the absorbances measured by scanning the sample image on the vidicon from top to bottom and from bottom to top, each scan beginning immediately after the laser was incident on the sample and taking 2.4 s to complete. The average time assigned to each of these frames is, therefore, 1.2 s. (*b–d*) Profiles obtained by scanning the vidicon face from bottom upward, taken at 1.2, 4.2, and 16.2 s (on the average), respectively, after the laser beam was incident on the sample. Note the difference between panels *a* and *b* of this figure. Because CO-diffusion out of the photolysed volume occurs on a time scale similar to the frame scan time, in panel *b* the horizontal extent of the photolysis profile appears bigger at the top of the frame (where the scan ended) than at the bottom (where the scan started). This apparent anomaly is absent in panel *a* because of the averaging procedure mentioned there.

$$y_1 = \Sigma\, y\Delta A(x, y) / \Sigma\, \Delta A(x, y) \qquad (5b)$$

The summations here are taken over the entire frame. The center so chosen is then checked by inscribing the largest circle entirely in the frame about that center and calculating a center again. If the center determined from the new restricted data set is different from that taken using the entire frame, the process is repeated until there is no change. Usually a single iteration sufficed. Once the center is known, the laser-scattered light can be normalized by dividing by the beam profile given by Eqs. 2–4, replacing x_0 and y_0 by x_1 and y_1.

Data Handling Procedures

Data colleciton is triggered when the net intensity in a given frame differed from the previous one by a present threshold, which was taken here to be 4% of the previous frame intensity. The limitations of the sweep rate for the vidicon dictate that at least 3 s must elapse between measurements. The control program allows a given number of scattering data frames to be collected, after which the ETFC begins alternation to collect scattering and birefringence.

The up-down averaging procedure (vide supra) could not be used to obtain an average frame time for the scattering and birefringence data because subsequent domains grew at different sample positions. Hence a correction was applied based on the sequence in which the pixels were read out from the vidicon. A weighted average was constructed from the intensity of a given frame and the frame before it, so as to give a new corrected frame in which all grid elements correspond to the same time. This corrected intensity is given by

$$I_{corr}(x, y, t_2) = f(x, y)\, I(x, y, t_1) + [1 - f(x, y)]\, I(x, y, t_2), \qquad (6a)$$

where

$$f(x, y) = [x\, \Delta t_x + y\, \Delta t_y] / \Delta T, \qquad (6b)$$

in which Δt_x is the time delay per x element (0.16 ms), Δt_y is the time delay per track y (47.24 ms), and ΔT is the total time between frames ($\Delta T = t_2 - t_1 = 3$ s).

To study the symmetry of the growing domain, each frame of normalized scattering and birefringence was analyzed by fourier transform, using a fast Fourier transform algorithm (Brigham, 1974). Symmetry was assessed about a domain center chosen in the following fashion. The peak-normalized intensity of the first scattering frame was taken as a trial center, and the largest circle about this center was then inscribed in the frame. Within that circle, a scattering centroid was calculated from Eq. 5, replacing ΔA by I_{norm}. The coordinates of this centroid were then taken as a new trial center, a new circle was drawn, and the process repeated until there was no difference in the trial center and the centroid coordinates.

Annuli of 4-μm thickness were contructed about the center as determined above, and each annulus was divided into 64 angular slices. Then the intensity of birefringence or normalized scattering can be written as

$$I(R_j, \theta) = \sum_{n=0}^{63} f_n(R_j) \exp(in\theta), \qquad (7)$$

where θ is one of the discrete set of 64 angles into which the entire annulus has been divided, and R_j is the mean radius of the annulus. The number of annuli used in a given experiment was limited by the largest circle about the domain center which intersected at most one boundary. (Equivalently, the circle of analysis could extend beyond only one edge of the data square.) When an annulus required data which was missing, it was "regenerated" by a rotation of π about the beam center. Because this procedure can generate false symmetry, we were careful to ascertain that any symmetry-based conclusion depended only on complete data sets. The value of the regenerated data is that is allows for improved resolution. The fourier transform data provided angular and radial data for subsequent anaysis. Of particular use is the amplitude of each of the various components,

$$F_n^2(R_j) = 1/2\, [f_n(R_j) + f_{-n}(R_j) f_n^*(R_j) f_{-n}^*(R_j)] \quad \text{for } n \neq 0 \qquad (8a)$$

and

$$F_0^2(R_j) = f_0(R_j) f_0^*(R_j), \quad \text{for } n = 0, \qquad (8b)$$

where the asterisk denotes the complex conjugate. The zero component is the intensity average. The amplitudes describe the symmetry of the domain. If we compute F_n/F_0, i.e., what fraction of F_0 appears in each component, we have a quantitative measure of the different symmetry compoents. We can then determine, for example, how fast a twofold symmetry decays. Because of the crossed polarizers, the birefringence will only contain even components.

RESULTS

The kinetics of 65 domains were studied in seven separate experiments. Desaturation measurements, beam profiling, and location control experiments were performed for each of these seven experiments. Fig. 4 shows typical results for an experiment with a stage temperature of 10°C, and laser power density of 0.51 kW/cm^2. The intensity of the collected light is shown as the third dimension, and the physical x and y directions are the coordinates of the plane. Because the maximum intensity of each frame is drawn as the same height, the net increase in absolute peak height of about an order of magnitude is not apparent. In the experiment shown here, data collection commenced when the light scattering signal changed by 5% of the background, and each subsequent scattering frame was collected when the intensity increased by 4% thereafter, or after a wait of 3 s, which is the minimum time between two successive vidicon scans. (The appearance of additional peaks in the scattering pattern was highly variable and was not analyzed further.) Six scattering frames were collected, whereupon the ETFC switched to monitoring on the 488-nm beam. Thereafter changes in the birefringence signal controlled the triggering, with threshholds again set at 4%. Whenever a frame of birefringence was triggered for collection, a frame at 514 nm was also collected. Although the maximum spatial extent of both birefringence and scattering was similar, the birefringence signal is notably less uniform than the scattering, which almost uniformly filled the frame. As the birefringence signal increased, the scattering intensity decreased markedly (although this is not so apparent in the figure because each frame is scaled by its maximum height).

It is evident that the birefringence pattern did not grow as the expected Maltese cross, but began as two pronounced lobes. In order to improve temporal resolution of the birefringence data, 16 domains were monitored with a sequence of scattering/birefringence collection which differed from the experiments described above. In these 16 experiments, the six initial scattering frames were replaced

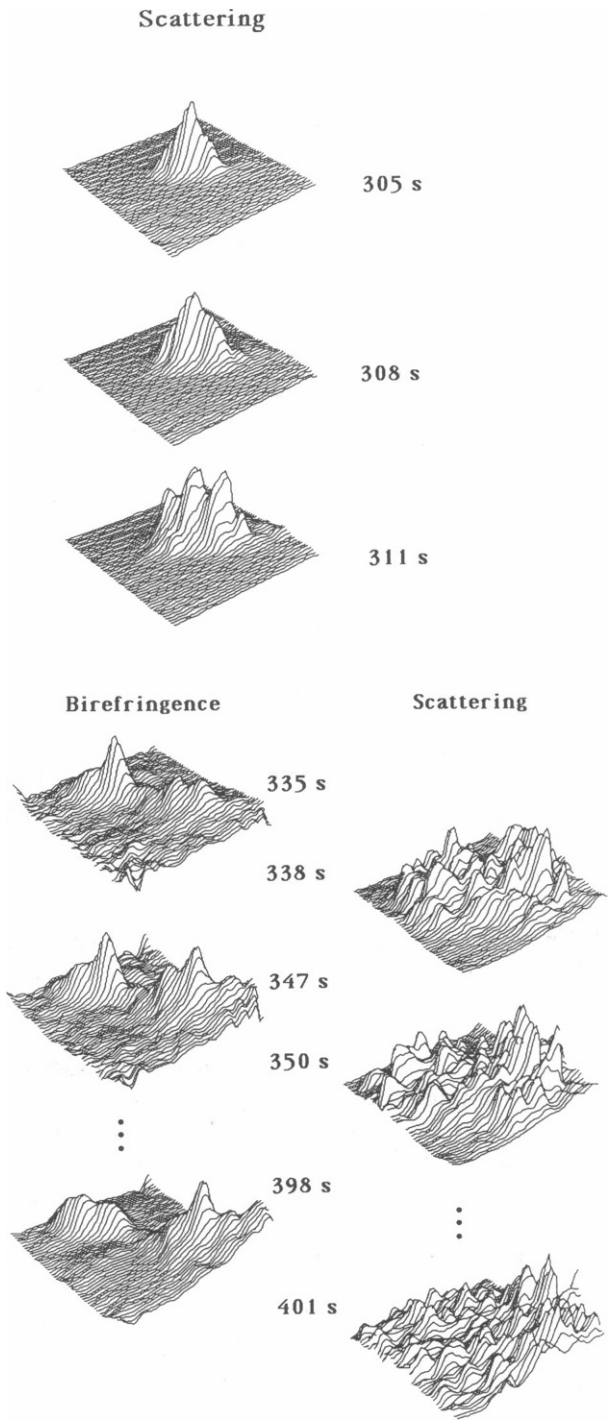

FIGURE 4 Typical data for a 0.313 g/cm^3 sample, with stage temperature of 10°C and power density of 0.51 kW/cm^2. Each frame shows the data relative to the highest intensity of the frame; actual heights of the scattering differ by approximately a factor of 10 between initial and final frames. Data collection was initially triggered when the background changed by 5%; subsequent frames, which were measured every 3 s, were saved when the mean intensity changed by 4% or greater. Six scattering frames were collected as quickly as possible, viz., 3 s apart, because of the rapid growth of scattering. At that time the ETFC changed to birefringence, whereupon changes in birefringence of 4% caused the data frame to be saved. Whenever a birefringence frame was saved, the ETFC changed filters, and a scattering file was also collected.

by a single frame of scattering (which set the delay time and fixed the beam center), whereupon the ETFC was switched to birefringence. This data did not present any particularly novel features. The maximum extent of the birefringence was about as large as the diameter of the scattering, and again the birefringence has a twofold symmetry while the scattering is roughly radially symmetric. Fig. 5 shows an experiment in which the birefringence was not only triggered early, but also allowed to incubate for a long time. The domain center was determined from the scattering data (not shown) and is marked in the figure. In time a third and eventually a fourth lobe appeared, as shown. When viewed by eye near the end of the experiment, this domain showed a well-formed, typical cross. This slow production of the cross pattern was evident whenever experiments were allowed to proceed to longer times.

The domain centers were distributed in no obvious

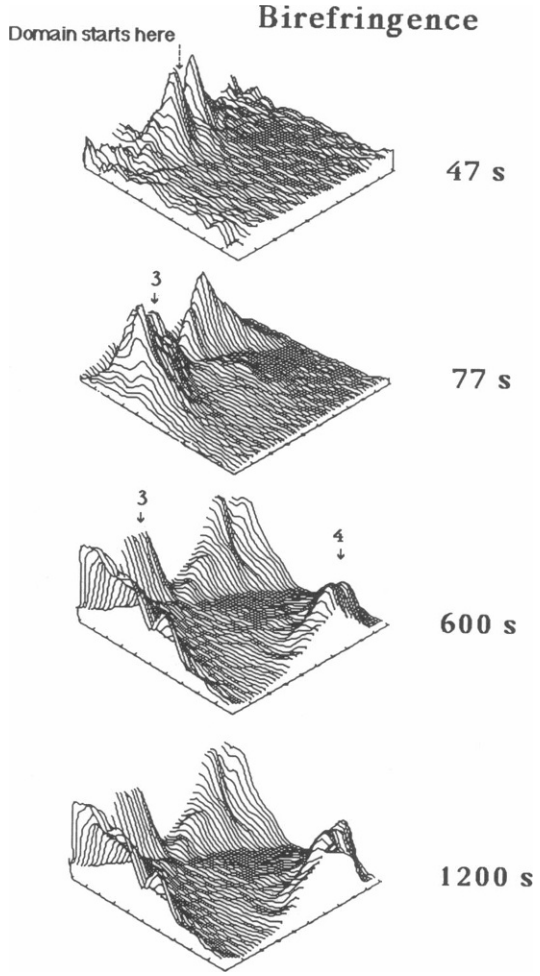

FIGURE 5 Evolution of the fourfold symmetry in birefringence. Scattering trigger occurred at 37.8 s, and the domain was centered at the location indicated. After the immediate appearance of the two-lobed pattern, a third lobe and ultimately a fourth appear. Stage temperature was 5°C, and laser power density was 0.74 kW/cm^2.

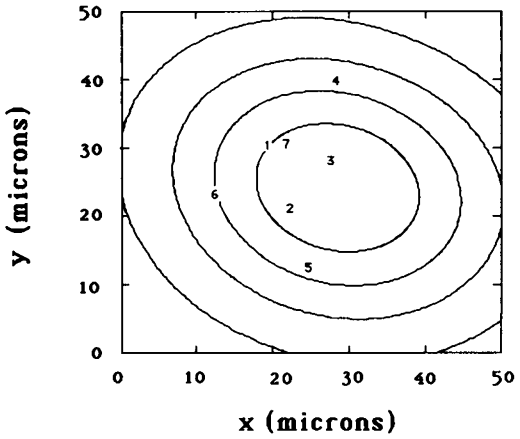

FIGURE 6 Location of domain centers on the photolysed area in seven consecutive polymerization events on the same sample; numbers refer to the sequence of the experiments. Also shown are contours representing the fit to Eqs. 2–4 of the laser beam intensity profile used in this experiment. This figure indicates that there is no correlation between the locations of the centers of domains that grew in successive experiments.

pattern, and in particular there was no distinct preference for the beam center. Fig. 6 shows the location of domains from other experiments on the same day as the data of Fig. 4; numbers refer to the sequence of their appearance. Also shown in the figure are the laser beam contours. In a number of experiments, multiple well-resolved domains were observed which proceeded to intersect. At this time no analysis has been prepared on what is likely to be an important facet of the polymerization process.

Symmetry Properties

In a noise-free environment, the symmetry of the growing domain would be evident upon inspection of the data of Fig. 4. Whereas there is some hint of symmetries in the data, a quantitative measure was desirable. A key question is whether the two-lobed pattern seen in birefringence has any counterpart in the scattering data. Annuli of 4-μm thickness were constructed about the domain center, and the Fourier transform computed of each annulus as described above (cf. Eqs. 7 and 8) This provides a quantitative description of the symmetry properties of the growing domain. Fig. 7 shows the amount of twofold component, normalized by the average intensity, (i.e., F_2/F_0) for five annuli for both scattering and birefringence for all the experiments. The data is shown for scattering and birefringence at equivalent times, namely the time when the birefringence is first observed. Because some domains form closer to the edge of the frame than others, there are not as many large annuli as there are small annuli. Birefringence is shown as the filled histogram while the scattering is shown as empty. The birefringence data is clearly dominated by the twofold component. Typically, the center of the cross pattern is dark, which shows up in this data as the absence of the strong twofold symmetry is the smallest

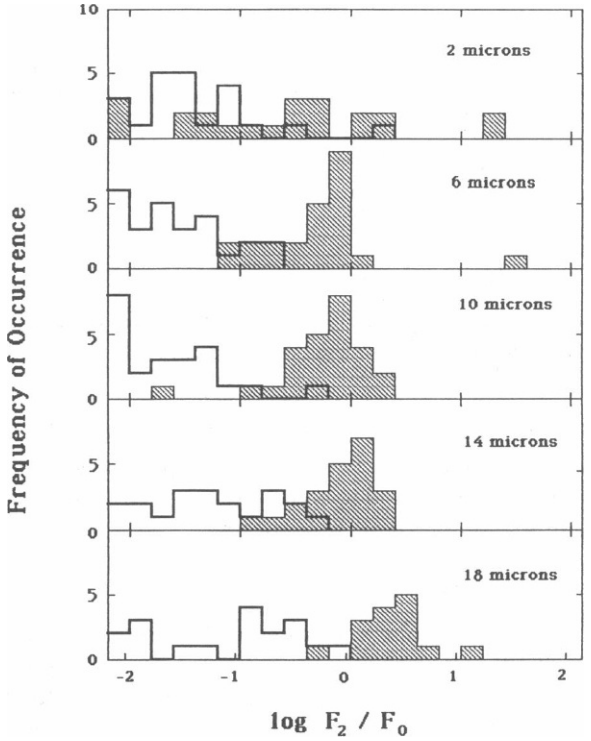

FIGURE 7 Comparison of the degree of spatial symmetry present in the scattering and birefringence signals at the time when birefringence is first triggered. F_0, defined by Eq. 8b, denotes the average of the analyzed data, whereas F_2 gives the total amplitude of the twofold component. By normalizing F_2 by F_0 the relative magnitude of the twofold component is shown. Birefringence is shown shaded; scattering is shown as the open histogram. There is only ~20% of the twofold component in the scattering data, whereas it dominates the birefringence data.

annulus of the birefringence. It is also intersting that the birefringence average of all the experiments exceeds unity at the largest annulus. This can only happen if another component, in this case the fourfold, has acted to diminish the twofold amplitude. It suggests the beginning of more symmetric alignment farther from the domain center.

In contrast to the above, only 18–22% twofold symmetry is seen in the scattering. This twofold scattering component slowly decreases throughout the experiment. All scattering annuli decrease their proportion of the twofold component in the first 3 s by ~17%. Table I shows the kinetics of the disappearance of twofold component. Each experiment was fit to an exponential decay, assuming that the twofold would ultimately disappear. All the decay rates were then averaged, weighted by their fitting errors. The scattering data shows well-determined decay rates, on the scale of kiloseconds. This can be viewed as the approach to uniformity.

We can also examine the kinetics of the birefringence symmetry. For birefringence, a uniform radial distribution would have all F_4 components. The appearance of F_4 in birefringence also occurs on the order of kiloseconds. Thus, although scattering, and birefringence begin with different

TABLE 1
RATE OF CHANGE OF RELATIVE MAGNITUDE OF TWOFOLD COMPONENT OF SCATTERING (F_2/F_0)

Distance	Rate*	
μm	ks^{-1}	
2	−0.98	±0.12
6	−6.43	±0.38
10	−6.91	±0.54
14	−10.70	±0.71
18	−8.47	±1.13

*Determined for the first six points in an experiment.

initial symmetry, both approach uniformity and do so with about the same rate. The twofold component of the birefringence is also found to be slowly diminishing, and with a roughly similar rate to the scattering.

Radial Profiles

A radial distribution is obtained if the Fourier transform amplitude corresponding to the average intensity (F_0) of scattering or birefringence is plotted as a function of distance from the center of the domain. Fig. 8 *a* shows such a radial distribution for the experiment from the series described above. The distribution can be fit by a gaussian form, i.e.,

$$\langle I_{scat} \rangle = I_{0,s} \exp [-(r/\sigma_s)^2]. \quad (9)$$

There is some systematic deviation of the lowest points from a gaussian shape, which may be due in part to the calibration difficulties described in Methods. Because the ordinate in Fig. 8 is logarithmic these deviations are quite small.

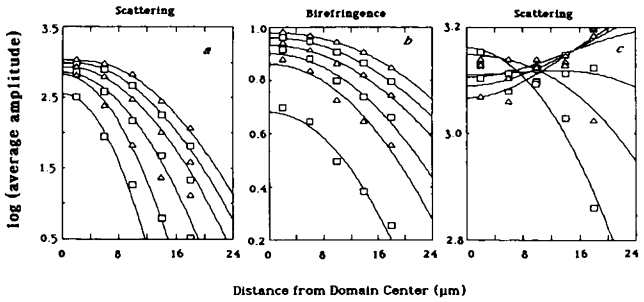

FIGURE 8 Radial profiles of the signals collected in the experiment shown in Fig. 4. For a given value of the abscissa, data points at increasing values of the ordinate in each panel correspond to increasing times in the data-collection sequence. (*a*) Profiles of the scattering signal (*squares and triangles*), fit to a gaussian form as given by Eq. 9 of the text (*solid line*). The profiles were collected 305, 308, 311, 314 and 317, and 320 s after photolysis was begun. (*b*) Profiles of the birefringence signal, fit to the sum of two gaussian forms with opposite signs, as given by Eq. 10 of the text. These profiles were collected 335, 347, 359, 374, 383, and 398 s after the initiation of photolysis. (*c*) Profiles of the scattering signal at times later than those depicted in panel *a*. Each of these profiles was collected 3 s after a corresponding birefringence profile shown in panel *b*. The solid lines show the fit of the data to the sum of two gaussian forms with opposite signs, one of which has its width determined by the fit to the appropriate birefringence profile in panel *b*.

The center panel (Fig. 8 *b*) shows the radial profile on the birefringence, which is also well fit by a gaussian. In this case, though, the radial profile is describing the radial behavior of a two-lobed structure. Because birefringence responds to the square of the concentration of aligned polymers (Hofrichter, 1976), the square root of the measured intensity I_{meas} is shown. The birefringence was fit with a sum of gaussians to account for the typically dark center (not evident in this figure). The broader gaussian gives the width σ_b used in the analysis. Thus the general equation used to fit the birefringence was

$$I_{biref} = [\langle I_{meas} \rangle]^{1/2} = I_{0,b} \exp [-(r/\sigma_b)^2] - I_{1,b} \exp [-(r/\sigma_c)^2] \quad (10)$$

When the birefringence appears, the scattering intensity begins to decrease at the domain center. The decrease is in absolute, not relative terms. Thus it does not result from central saturation plus growth of outer areas. Fig. 8 *c* shows the scattering data which corresponds to the birefringence data of Fig. 8 *b*. If the decrease is scattering is assumed to arise from the same phenomena that produce the birefringence, the scattering can be described by a sum of gaussians

$$I_{scat} = I_{0,s} \exp [-(r/\sigma_s)^2] - I_{1,s} \exp [-(r/\sigma_b)^2], \quad (11)$$

in which the second term has a positive amplitude $I_{1,s}$ and a width σ_b determined by the fit to the birefringence with Eq. 10. The curves in Fig. 8 *c* have been calculated with such a procedure, fitting the radial scattering profiles by Eq. 12 varying the three parameters $I_{0,s}$, σ_s, and $I_{1,s}$. As is apparent from the figure, this procedure works well in reproducing the data.

Fig. 9 shows the time course of the parameters obtained by this gaussian fit of the data set of Fig. 4. The scattering amplitude $I_{0,s}$ rises and rapidly saturates. The curve through the data shows a fit of saturating exponential, viz.,

$$I_{0,s} = I_{max,s}\{1 - \exp [-k_{sat,s}(t - t_s)]\}. \quad (12)$$

Three parameters were varied in these fits: $I_{max,s}$, $k_{sat,s}$, and t_s. The latter is needed because, due to stochastic fluctuations in the nucleation process (Ferrone et al., 1980; Ferrone et al; 1985a; Hofrichter, 1986), the time at which nucleation occurs is not the time at which the experiment began. This procedure fit the data well. Typical values of t_s were ~1 s before the first triggered frame.

The amplitude of the second (decreasing) gaussian $I_{1,s}$ is also plotted with the scattering amplitude, and is much smaller. The last two or three points of the scattering data have such large gaussian widths σ_s relative to the frame size that the parameters are not well determined, and those parameters are shown as dotted symbols. Whereas $I_{0,s}$

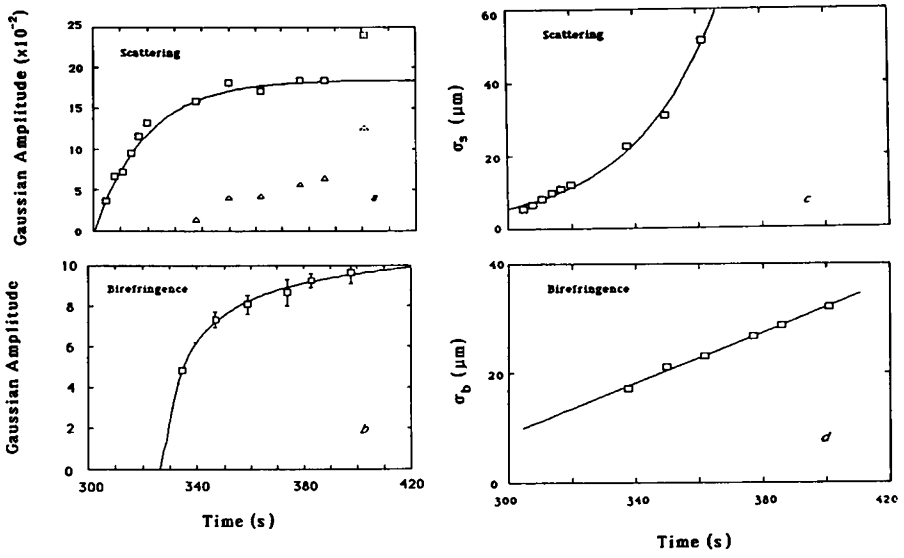

FIGURE 9 Time dependence of the parameters used to fit the radial profiles shown in Fig. 8. (*a*) Amplitudes of the gaussian fit to the scattering profiles: squares represent the amplitude $I_{0,s}$, which accounts for the increase in scattering with time shown in Fig. 8 *a*, whereas the solid line is the fit to Eq. 12 of the text with the parameters $I_{max,s} = 12.4$, $K_{sat,s} = 0.063\ s^{-1}$, $t_s = 302$ s. Triangles represent the amplitude $I_{1,s}$, which accounts for the decrease in the scattering apparent in Fig. 8 *c*. (*b*) Amplitudes of the gaussian fit to the birefringence profiles, fit to Eq. 13 of the text with the parameters: $I_{max,b} = 12.4$, $k_{sat,b} = 0.29\ s^{-1}$, $t_s = 326$ s. (*c*) Gaussian widths of the scattering profiles. The size of the domain as given by this width is seen to accelerate. This data is fit to an exponential form given by Eq. 15 of the text. (*d*) Gaussian widths of the birefringence profiles. This width clearly increases linearly with time and is fit to a linear form given by Eq. 14 of the text.

appears to have saturated, the amplitude $I_{1,s}$ displays a slow growth.

The birefringence amplitude $I_{0,b}$ shows a rapid rise followed by a slower, steady increase that parallels the increase in $I_{1,s}$. The long, slow birefringence tail cannot be described by an equation of the type of Eq. 12. From considerations to be described in the discussion (also see Appendix), we sought to fit the data with a diffusionlike time dependence. Thus we fit the birefringence amplitude by the equation

$$I_{0,b} = I_{max,b}(1 - erf\{[k_{sat,b}(t - t_b)]^{-1/2}\}). \quad (13)$$

This did an excellent job in fitting in birefringence data, as can be seen in Fig. 9. Fig. 10 shows an experiment in which the birefrigence amplitude was followed for a long time, corresponding to the data of Fig. 5, fit by this equation. Again, the fit is excellent.

From Fig. 9 it is apparent that the width of all the gaussians increases with time. (If they did not, each subsequent one would resemble the previous one vertically translated.) The width for the birefringence expands steadily and is well fit by a straight line.

$$\sigma_b = \sigma_{0,b} + v_b t. \quad (14)$$

In contrast, the width for the scattering data accelerates, and can be described by an exponential of the form

$$\sigma_s = \sigma_{0,s}[\exp(k_s t) - 1]. \quad (15)$$

The acceleration extends across the region in which Eq. 11 (two gaussians) has replaced Eq. 9 with a single gaussian. These features are seen in all the data sets, and the acceleration is observable even when only a single gaussian analysis is used (i.e., before birefringence has occurred.)

Of the four rates measured in the above analysis (k_s, $k_{sat,s}$, v_b, and $K_{sat,b}$) only v_b had an effective activation energy significant from zero. Effective activation energies were determined by a linear fit of the ln(rate) vs. $1/T$. The activation energy for v_b is found to be 10 ± 4 kcal/mol. For other parameters, large error bars included zero activation energy. The source of the large uncertainty is not clear but may arise from assumptions implicit in the averaging process that leads to the radial profiles.

DISCUSSION

The phenomenological picture of domain growth is complex. The scattering signal first observed is primarily symmetric and grows in all directions about the center of the domain. Birefringence begins with a twofold pattern which only later evolves the characteristic fourfold cross pattern. The light scattering signal goes through a maximum, followed by a spatially distinct decrease whose size

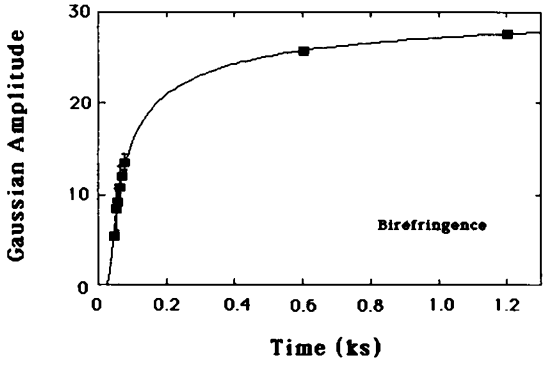

FIGURE 10 Gaussian amplitude of the birefringence signal measured for a much longer period than shown in Fig. 9, showing saturation as predicted by Eq. 13 of the text. The parameters that best fit this data to Eq. 13 are: $I_{max,b} = 31.9$, $k_{sat,b} = 0.054\ s^{-1}$, $t_s = 292$ s.

and temporal behavior correspond with the size and growth of the birefringence. The characteristic size of the domain as seen by light scattering accelerates, whereas the aligned portion of the domain expands linearly. The radial profiles of scattering and birefringence are roughly gaussian. In the first part of this discussion, we shall describe the initial structure of the domain. In the second section, we turn to the kinetics of the domain formation process wherein we specifically deal with the scattering decrease and the process of alignment. Finally, we deal with the implications of these findings.

Domain Structure

From the observation of light scattering described above, the mass of polymers that constitute a domain expand radially with no strong symmetry axes. (About 20% of the signal is in twofold patterns.) This is consistent with results obtained at or near equilibrium which qualitatively show circular symmetry (White and Heagan, 1970; Beach et al; 1988; Hofrichter, J., unpublished observations). However, at equilibrium the domain is composed of radially aligned polymers, whereas initially the domain is not well aligned, as is evident from the small birefringence shown above. Scattering and birefringence can be usefully compared at the time when the domain scattering has become saturated. At that time the intensity of the birefringence is small, and it is shaped in a twofold bowtie pattern. In times of the order of 200 s, birefringence assumes a full maltese cross pattern, and the amplitude has increased by a factor of 4 or 5. Thus the aligned polymers seen at scattering saturation represent only 22 ± 11% of the fully aligned sample. The implication is that a large mass (75–80%) of the polymers are unaligned when the scattering has saturated. Hence, the initial structure of a domain is quite different from its final appearance, and the alignment into spherulites must be a later occurrence.

In comparing birefringence and scattering amplitudes, we have implicity assumed that both signals are linear and can be calibrated against their peak values. (The birefringence signal is of course adjusted for its squared relation of polymers to intensity.) This linearity is supported by several observations. The scattering signal reaches a maximum and decreases; this was also observed in a similar geometry in previous studies, and suggests upon first glance that the relationship between polymer mass and scattering is highly nonlinear. (Ferrone et al., 1985*a*). However, an important observation from those studies is that the time for the decay after the peak was far less sensitive to concentration than the delay time. Thus, samples gelled in milliseconds exhibited a decay on the scale of seconds. If the decay was solely due to drastic nonlinearity in the response of the scattering to polymer mass, then a sample which exhibited rapid growth would arrive at the nonlinear or inverted response region quickly, and the decay would have been rapid. Hence we can exclude any strong nonlinearities leading to inversion of the signal. Two observations from the present data provide additional support for approximately linear response. Similarity in the symmetry components between birefringence and scattering argues that the two types of signal scale alike, for, at the time of scattering saturation, the birefringence has twofold symmetry and represents 22% of maximum alignment; while at the same time, the scattering data shows a twofold symmetry component which is 18–25% of its maximum. Finally, the scattering signal decrease has a gaussian width which matches the gaussian width of the birefringence. If the two signals were not both approximately linear, this correspondence would be most unlikely. Thus the assumption of linearity employed above appear reasonable.

Domain Kinetics

We next turn to a consideration of the kinetic features seen here. A detailed kinetic model for the radial growth of domains based on the double nucleation model (Ferrone et al., 1985*b*) is the subject of a separate paper (Zhou, H.X., and F.A. Ferrone, submitted for publication). Here we wish to examine the interrelationship of scattering and birefringence signals. Although there are drastic differences in the two signals (e.g., the twofold character of birefringence whenthe scattering is symmetric), the systematic behavior of the two signals is very similar.

The transition to the radial arrays occurs at the expense of the twofold component, and the unaligned component as well. From analysis of the aligned polymers seen by birefringence, typical time for the approach to (isotropic) saturation is 193 (±48) s. The time for scattering to assume isotropic form (i.e., for the twofold component to disappear) is ~150 s (Table I). Thus the increase in birefringence signal matches the decrease in twofold scattering. As seen in the radial profiles above, the growth in the birefringence is also accompanied by a decrease in overall scattering. These two probes have the same spatial and temporal evolution. Hence it is clear that a specific, localized process occurs which transforms the initial domain into a spherulite.

A plausible mechanism which unifies much of the data is based on a postgrowth lengthening process. This works in the following way. After polymers have formed, and the local monomer concentration reaches its equilibrium value, monomers will continue to associate and dissociate from the end of polymers. This random process has a certain probability of entirely dissociating a polymer. This mechanism for polymer destruction is not matched by a creation mechanism. Due to the high concentration dependence of the nucleation process, nucleation is greatly suppressed at regions of the sample which have some monomer depletion, and virtually nonexistent at equilibrium. (For example, reduction of the monomer concentration by only 1% decreases the rate of heterogeneous nucleation by ~60% at 25°C [Ferrone et al., 1985*b*].) As some polymers are lost, the remaining polymers must lengthen to keep the poly-

merized monomer concentration constant. A slow lengthening process will therefore occur. (A full derivation is presented in the Appendix.) Ultimately this mechanism would lead to a single long fiber. However, other slow processes such as polymer breakage or nucleation will occur to establish an equilibrium. We will show in turn how the lengthening process explains the decrease in light scattering and, with an additional assumption, the alignment which produces birefringence.

Scattering Decrease. We contend that the observed decrease in scattering intensity is not due to less total scattering, but rather to a change in angular dependence which causes less light to be scattered into our detector while more light is scattered into unobserved regions. Polymer length affects not only total scattering cross-section but also angular dependence. Short polymers will scatter over a large angular spread, and so most short polymers will produce some scattering into the detector. In contrast, long (infinite) cylinders scatter light into a cone with the apex half angle equal to that of the incident angle (Kerker, 1969; van de Hulst, 1981; Cohen, et al; 1983) Only some of the scattering of such polymers will be collected in our backscatter geometry and thus some polymers will be unseen. As the polymers lengthen, then, scattering intensity decreases becuase of light scattered out of the detection cone.

An order of magnitude estimate of this effect, including the cross-section differences, supports this interpretation. Typically, rods with radius a will scatter more efficiently (i.e., have a larger total cross-section) than spheres of the same radius by roughly a factor of λ/a (van de Hulst, 1980). Thus long polymers of HbS will scatter more efficiently overall (λ/a = 514 nm/10 nm = 51) than the same number of molecules assembled into polymers with length equal to the diameter. However, angular factors reduce the light which layers randomly oriented long rods scatter into our detection geometry, (which collects ~1 steradian), by a factor of $\sim 10^3$. Bishop, Marilyn F., personal communication). In contrast, Rayleigh scattering from spheres would be roughly isotropic, and so sphere scattering angular factors would only reduce the intensity observed in our geometry by a factor of 4π. Hence the rod (polymer) scattering is $\sim 51 \times 4\pi \times 10^{-3} = 0.6$ as great as that of the same material in short polymers. Of course, the short polymers will themselves scatter more than the monomers by a factor of 200 (that being the number of monomers in this specific short polymer where length equals diameter). Thus, based on angular scattering factors, and a lengthening process, a maximum in the light scattering can be rationalized.

In previous studies with the same geometry, it was observed that a scattering decrease occurred for all samples, whether polymerized in milliseconds or in kiloseconds (Ferrone et al., 1985*a*). However, the scattering decrease occurred with about the same rate in all cases. This follows from the explanation given here, because the rate depends on the equilibrium concentrations, rather than the initial concentrations of monomers.

This explanation also rationalizes other observations. It implies that in turbidity little overshoot should be seen, as is observed (Eaton et al, 1976*b*; Sunshine et al, 1979; Ferrone et al., 1985*a*). It further implies that much more light would be scattered into the forward angle, which has also been observed (Hofrichter, J., personal communication). An attempt to make this theory more quantitative is severely hampered by a lack of understanding the optical properties of the dense, multiple scattering regime. Even in the dilute scattering limit utilized in the preceding approximations, it is notable that interference effects can occur for particles with a dimension near the wavelength of light. These resonance or interference effects are difficult to describe without a full calculation, and may also play a role in the phenomena observed here (Kerker, 1969; van de Hulst, 1981).

Alignment. The scattering signal begins to decrease as the birefringence signal appears, suggesting a connection between polymer alignment and the lengthening process described above. A simple model shows how such a connection can be formulated. We make the assumption that there are two classes of polymers: those which are entangled, and cannot grow, and those aligned radially, which can grow. Becasue the entangled polymers are interspersed among the radial polymers, there is no net birefringence. Because the center of the domain is likely to be dense, due to growth inwards from polymers nucleated at distances away from the center, the outward radial direction presents a likely choice for less entangled growth. In this picture, then, the appearance of birefringence can be thought of as the result of disappearance of the nonproductive entangled polymers. (Lengthening of the polymers already radially aligned will also occur, but it does not increase the birefringence because it merely changes the number of polymers, not the overall concentration of polymerized monomers.)

From this model we can drive an expression for the monomers transferred from entangled to radial monomers. If all the entangled polymers had length x_0 initially, the birefringence will be proportional to the transferred monomers, and grow as $\{1 - erf[x_0/\sigma(t)]\}$, where $\sigma(t)$ is the width of the distribtuion that results from the length redistribution process. As shown in the Appendix, $\sigma^2(t) = 4k_+\gamma_s c_s t$, where k_+ is the monomer addition rate constant, c_s is the solubility, and γ_s is the activity coefficient at solubility. This implies that the birefringence should grow with a diffusionlike $\sqrt{t}$ rate, as given by Eq. 13. Whereas the model used here assumes that all the polymers initially have the same length, a more realistic model using a distribution of lengths introduces additional parameters and an additional assumption (viz., the shape of the distribution). Our strategy is to show that the simple approach fits the data. If so, a distribution should also be able to describe the data. As is apparent from Figs. 9 and

10, the function described by Eq. 13 fits the birefringence much better than a typical exponential saturation function. Similar birefringence progress curves have been observed previously (Hofrichter et al., 1974; Ross et al., 1975) in multidomain samples.

The connection between birefringence and scattering then arises becuase both processes are driven by the same kinetics. In rapidly polymerized multidomain samples, no birefringence is observed although a scattering maximum does appear. This can be understood as the result of the polymers of one domain entangling with another. In this case, growth along a radial direction is not significantly less entangled, and no birefringence appears.

This explanation also predicts that the birefringence should lag the scattering, which we also observe. The size of the lag can be calculated from the model here, by determining when the function given by Eq. 13 reaches 10% of its final value. This equation predicts a delay of $\sim\frac{1}{3}k_{sat,b}$, which is ~60 s. Because this value depends on the monomer addition rate and the solubility, (cf, Appendix) rather than initial conditions, it will be a universal rate for all experiments done at the same temperature, and will vary only due to temperature effects. Moreover, because the addition rate increases with temperature while the solubility decreases, the two effects oppose one another. At first sight this appears to contradict other observations which found that delay times measured by birefringence were the same as seen by other techniques such as turbidity and calorimetry (Ross et al., 1975; Eaton et al., 1976*b*). However, those observations were made for much slower gelation, in which case the extra 1-min delay predicted here would have gone unnoticed.

The presence of twofold symmetry in birefringence and scattering is also rationalized. The regions that align have been polymerized for the longest time. Because the scattering begins with a twofold symmetry, the formation of birefringence in a twofold pattern should be the consequence of the relative age of that region of the sample.

The proposed monomer redistribution mechanism is also quantitatively consistent. Let us first examine the size of the polymers that are lost in the alignment transformation that leads to birefringence. In our admittedly oversimplified model, the polymers with x_0 monomers disappear with characteristic times given by $x_0^2/(4k_+\gamma_s c_s)$. Using the value of k_+ of 6.3 $mM^{-1}s^{-1}$ (Hofrichter, 1986), and the characteristic time of 193 s, the average size of polymers is found to be ~0.12 μm. This is reasonable from two points of view. First of all, this size will be much closer to the small scatterer (Rayleigh) limit than the infinite polymer limit. Secondly, the size fits well within the growing domain. If an average redistribution curve were constructed from an ensemble of polymer lengths, the dependence on x_0^2 will cause the shorter polymers to dominate the rate. Hence the value deduced for x_0 here is most likely a low estimate.

Another quantitative check comes from the rate at which the scattering approaches saturation. If the concentration of polymer ends is c_p, then the effective rate of approach to equilibrium is (Ferrone et al., 1985*b*)

$$k_{sat,s} = k_+ c_p \gamma_s (1 + \mathrm{d} \ln \gamma_s / \mathrm{d} \ln c_s). \quad (18)$$

This assumes that the rate $k_{sat,s}$ determined by fitting Eq. 12 to the gaussian amplitudes observes the polymerization at sufficiently long times to allow c_p to be regarded as a constant and permit γ to be approximated by γ_s. The average effective rate $k_{sat,s}$ in the experiments reported here is 0.17 s^{-1}. From this, c_p is found to be 1.5 μM. Coupled with the concentration of polymerized monomers, this implies that the average polymer size was 1.2×10^3 monomers, or 0.52 μm. This is in good agreement with the above estimate considering the rough nature of the calculation of the alignment transition rate. Furthermore, Eq. 18 refers to the concentration of polymers that are growing. If some fraction are entangled, then only some of the polymers present are growing. Hence this calculation underestimates the concentration of polymers ends and accordingly overestimates the average polymer length.

Implications

It is intriguing that the alignment process begins with twofold symmetry and then spreads to full radial symmetry. This could be the result of domain growth about the direction of the very first polymer. Further simulations of the secondary nucleation process are underway to attempt to relate this anisotropy to potential constraints on the secondary nucleation process. The gaussian nature of the profiles and their accelearation follow naturally from the double nucleation mechanism (Zhou, H. X., and F. A. Ferrone, submitted for publication). Thus, the observations presented here are consistent with the double nucleation mechanism of polymer formation. (Ferrone et al., 1980, 1985*a*).

From the data presented here, it is clear that growth and alignment are distinct processes. Initially polymer domains form as an entangled polymer mass. Alignment of the polymers into a spherulitic domain occurs only later in the process of domain formation. However, both alignment and growth are related to monomer addition rates, i.e., alignment occurs in this model by the loss of unaligned polymers, not by gross polymer motion. It is difficult to rule out the gross movement of polymers as a competing explanation for alignment, because no theory of those kinetics is known to the authors which applies in this concentrated polymer limit. The thermodynamic behavior of coupled alignment-elongation systems has been investigated by Briehl and Herzfeld (1979; Herzfeld and Briehl, 1981*a* and *b*) who found significant differences when polymers were allowed to change length. Whereas those findings are suggestive of alternative pathways to alignment via monomer exchange, they do not explicitly provide a kinetic rationale to show the relationship between fixed and variable length rod alignment kinetics. For more dilute

polymer systems, approximate theories do exist (Doi and Edwards, 1986) which can provide a rough lower limit on the rate of rotational diffusion. By such theories, sickle hemoglobin polymers of 0.5 μm length could be expected to rotate with characteristic times of ~260 s (where the rotation time is taken as the reciprocal of the rotational diffusion constant). In the dense polymer limit, therefore, one expects much longer times. Also, it is interesting to note that the rotational diffusion time depends on the seventh power of the fiber length. If such a length dependence persisted into the dense polymer regime, then the above alignment mechanism might entail the decrease in polymer length below a critical threshold to allow rotation rather than complete disappearance of entangled, nonradial polymers.

Because the lengthening of polymers occurs as the result of loss of short polymer through the rate $4k_+\gamma_s c_s$, lowering the solubility by use of high phosphate buffers (Adachi and Asakura, 1978, 1979, 1983), should show a much slower rate of scattering decrease, all other things being equal. (It should be noted that the Onsager criterion for alignment of rods, viz., that the rod volume fraction be greater than the ratio of diameter over length, may not be met at high phosphate conditions, so that there may be no thermodynamic driving force to align polymers.)

The spatio-temporal behavior of domains may have important clinical implications. Polymer alignment will affect both the internal structure of domains and the domain–domain interactions. Recent work by Danish et al. (1987), has found that the rheologic behavior of deoxy HbS gels depends on sample history; in particular, when samples were allowed to anneal they developed increased rigidity. Such mechanisms as discussed here could serve to anneal or align the interdomain polymers to give rise to such behavior. This is in general agreement with theoretical studies which have found that the stress-strain curves of rodlike polymer gels depends sensitively on their degree of alignment (Doi and Kuzuu, 1980).

In addition to the kinetic factors involved in the formation of polymers, which have been proposed as determinants of the severity of disease and the frequency of crises (Eaton et al., 1976*a*; Eaton and Hofrichter, 1987) the kinetics of domain alignment may also play a role. It has been suggested that a large number of cells may constantly sickle in the capillary system in "microcrises" (Ferrone et al., 1986). In that case, additional factors such as the number of domains or their state of alignment may be the deciding variables in precipitation of sickle crises and/or the severity of the disease (Ferrone, 1989).

APPENDIX

Elongation of Polymers

We can rationalize the increase of the average length of polymers in the following way. At equilibrium, the monomer concentration is c_s, with activity coefficient γ_s. There the elongation and monomer loss rates are equal, i.e.,

$$k_+\gamma_s c_s = k_-. \tag{A1}$$

A polymer of initial size (length) x_0 will undergo random size fluctuations about its mean size, x_0. This is analogous to a random walk on a line representing polymer size, with elementary steps given by the rate above. An ensemble of polymers all beginning with initial length x_0 will develop a distribution of lengths. This is analogous to diffusion from a point source in which an initial delta function spreads into a gaussian whose width increases with time. The probability of finding a polymer with size x having begun at x_0 therefore is

$$P(x, x_0) = (\sqrt{\pi}\sigma)^{-1} \exp[-(x - x_0)^2/\sigma^2]. \tag{A2}$$

This needs to be modified, however, to account for the fact that zero represents an absorbing boundary. Once a polymer reaches zero size it disappears and cannot enlarge. The gaussian of Eq. A2 includes contributions from random walk paths which have passed into a forbidden region (<0) and returned. To correct this, we can introduce an image distribution centered at $-x_0$, which we subtract. (For a full justification, see van Kampen [1981]). Thus Eq. A2 becomes

$$P(x, x_0) = (\sqrt{\pi}\sigma)^{-1}\{\exp[-(x - x_0)^2/\sigma^2] - \exp[-(x + x_0)^2/\sigma^2]\}. \tag{A3}$$

The width parameter, σ, is related to the number of steps in the walk, and it will increase as the number of steps of addition or loss increases. The average length of a distribution beginning from x_0 is simply

$$\langle x, x_0\rangle = \frac{\int_0^\infty x P(x, x_0)\, dx}{\int_0^\infty P(x, x_0)\, dx}. \tag{A4}$$

The denominator is needed because P is not normalized, since polymers can disappear. Evaluating the integral we find that the denominator has the dominant effect (i.e., the disappearance of polymers affects the average far more than the cutoff of the integral.) Thus we can write to a good approximation,

$$\langle x, x_0\rangle = x_0/erf(x_0/\sigma), \tag{A5}$$

where *erf* is the error functon, defined as

$$erf\, z = 2\pi^{-1/2}\int_0^z \exp(-u^2)\, du. \tag{A6}$$

When σ is small, $\langle x, x_0\rangle = x_0$, whereas when σ is much larger than the initial size, i.e., when the gaussian has spread to the origin, we get $\langle x, x_0\rangle = \sigma/(2\sqrt{\pi})$, in which all trace of the initial size has been lost, and the average size is determined by the spread of the curve. Thus elongation occurs.

Suppose that two classes of polymers exist: entangled or nonradial, and unentangled radial. Then both groups of polymers will undergo loss, but only the radial polymers elongate. If all the entangled polymers had length x_0, then there would be a transfer of the lost polymers, which would equal $x_0\{1 - erf[x_0/\sigma(t)]\}$.

Similar phenomena occur when there is an initial distribution of lengths. For the typical case in which polymers begin with an exponential distribution with average length L, i.e.,

$$p(x_0) = 1/L \exp(-x_0/L). \tag{A7}$$

The average length as time evolves is defined as

$$\langle N\rangle = \int_0^\infty \langle x, x_0\rangle p(x_0)\, dx_0. \tag{A8}$$

The plausibility of an exponential distribution for the double nucleation mechanism is justified in a brief derivation below. To simplify the integral, we adopt the approximation that

$$erf(y) = \begin{cases} 1 & y > 1 \\ y & y < 1. \end{cases} \quad \text{(A9)}$$

Because the average length of the exponential distribution is L, we can compare $\langle N \rangle$ to L. Then we get

$$\langle N \rangle / L = \exp(-r)(r+1) + (\sqrt{\pi}/2)\, r\, [1 - \exp(-r)], \quad \text{(A10)}$$

where $r = \sigma/L$. For small r, $\langle N \rangle / L$ becomes 1, whereas for large r it becomes $(\sqrt{\pi}/2)\, r$. Because σ increases with time, so will r, and the above equation then shows the increase in size for an exponential distribution of sizes.

To continue the description of the widening distribution of polymers as a diffusive process, we can formally identify as the diffusion constant the monomer step rate at equilibrium, i.e., $k_+ \gamma_s c_s$. Then,

$$\sigma^2(t) = 4 k_+ \gamma_s c_s t, \quad \text{(A11)}$$

so that taking $k_+ = 6.3\ \text{mM}^{-1}\,\text{s}^{-1}$ (Hofrichter, 1986) and $c_s = 2.76$ mM (Ross et al., 1977) so that $\gamma_s = \gamma(c_s) = 4.51$, we find $\sigma^2(t) = 3 \times 10^2\,\text{s}^{-1}\, t$.

Exponential distributions of polymer lengths have been seen in various polymer formation processes (Oosawa and Asakura, 1975; Mann, 1988). In the case of a nucleation process with a secondary pathway (cf., Bishop and Ferrone, 1984), it is easy to see that under simplifying conditions an exponential distribution will also result. If the polymer length distribution is given by $\Lambda(x, t)$, then there are two effects to consider, viz., propagation of existing polymers and creation of new polymers. Propagation means that if in time τ a polymer will grow by length x, then

$$\Lambda(x, t + \tau) = \Lambda(0, t). \quad \text{(A12)}$$

This assumes no monomer consumption, which is a reasonable assumption for the initial part of the curve, or for polymers at the domain frontier. Meanwhile, new polymers are also being added. Because polymers are created as "zero length," the probability of finding those will be proportional to the total length of polymers. Thus,

$$\Lambda(0, t) = \beta^2 \int_0^\infty x \Lambda(x, t)\, dx, \quad \text{(A13)}$$

where β^2 is a constant. The solution of these equations is

$$\Lambda(x, t) = \Lambda_0 \exp \beta (vt - x), \quad \text{(A14)}$$

where v is the rate of elongation of a given polymer. In more conventional terms, $v = k_+ \gamma c$. As expected for such a secondary-nucleation mechanism, the net polymer concentration increases exponentially. Clearly, the length distribution is a decaying exponential, with average polymer size given by β^{-1}.

The authors thank Mr. Huan Xiang Zhou for assistance with the plotting package, Mr. Anthony J. Martino for assistance in preparation of the hemoglobin, and Mr. Michael Cho for assistance with the heating calculation. Dr. Marilyn F. Bishop generously provided us with results of her light scattering calculations. Discussions with Dr. Leonard Cohen and Dr. Judith Herzfeld were also helpful. Finally, we are especially grateful for the expert electronics and computer assistance of Mr. Wolfgang Nadler.

This work was supported by the National Institutes of Health through grant HL28102.

Received for publication 16 December 1987 and in final form 8 June 1988.

REFERENCES

Adachi, K., and T. Asakura. 1978. Demonstration of a delay time during aggregation of diluted solutions of deoxyhemoglobin S and hemoglobin C_{Harlem} is concentrated phosphate buffer. *J. Biol. Chem.* 253:6641–6643.

Adachi, K., and T. Asakura. 1979. Nucleation-controlled aggregation of deoxyhemoglobin S. Possible difference in the size of nuclei in different phosphate concentrations. *J. Biol. Chem.* 254:7765–7771.

Adachi, K., and T. Asakura. 1983. Multiple nature of polymers of deoxyhemoglobin S prepared by different methods. *J. Biol. Chem.* 258:3045–3050.

Basak, S., and F. A. Ferrone. 1988*a*. A simple, externally triggered filter changer. *Rev. Sci. Instrum.* 59:505–506.

Basak, S., and F. A. Ferrone. 1988*b*. Numerical linearization of a SIT vidicon response. *Rev. Sci. Instrum.* 59:1423–1425.

Beach, D. A., C. Bustamante, K. S. Wells, and K. M. Foucar. 1988. Differential polarization imaging. III. Theory confirmation. Patterns of polymerization of hemoglobin S in red blood cells. *Biophys. J.* 53:449–456.

Bevington, P. R. 1969. Data Reduction and Error Analysis for the Physical Sciences. McGraw Hill, New York. 232–242.

Bishop, M. F., and F. A. Ferrone. 1984. Kinetics of nucleation controlled polymerization: a perturbation treatment for use with a secondary pathway. *Biophys. J.* 46:631–644.

Briehl, R. W., and J. Herzfeld. 1979. The tactoidal state and phase transitions in systems of linear polymers of variable length. *Proc. Natl. Acad. Sci. USA.* 76:2740–2744.

Brigham, E. O. 1974. The Fast Fourier Transform., Prentice-Hall, Englewood Cliffs, NJ.

Cohen, L. D., R. D. Haracz, A. Cohen, and C. Acquista. 1983. Scattering of light from arbitrarily oriented finite cylinders. *Appl. Optics.* 22:742–748.

Coletta, M., J. Hofricther, F. A. Ferrone, and W. A. Eaton. 1982. Kinetics of sickle haemoglobin polymerization in single red cells. *Nature (Lond.)* 300:194–197.

Danish, E. H., J. W. Harris, C. R. Moore, and I. M. Krieger. 1987. Rheologic behavior of deoxyhemoglobin S gels. *J. Mol. Biol.* 196:421–431.

Doi, M., and S. F. Edwards. 1986. The Theory of Polymer Dynamics. Clarendon Press, Oxford.

Doi, M., and N. K. Kuzuu. 1980. Nonlinear elasticity of rodlike macromolecules in condensed state. *J. Polym. Sci. Polym. Phys.* 18:409–419.

Dykes, G., R. H. Crepeau, and S. J. Edelstein. 1978. Three dimensional reconstruction of the fibres of sickle cell haemoglobin. *Nature (Lond.).* 272:506–510.

Eaton, W. A., J. Hofrichter and P. D. Ross 1976*a*. Delay time of gelation: a possible determinant of clinical severity in sickle cell disease. *Blood.* 47:621–627.

Eaton, W. A., J. Hofrichter, P. D. Ross, R. Tschudin, and E. D. Becker. 1976*b*. Comparison of sickle cell hemoglobin gelation kinetics measured by NMR and optical means. *Biochem. Biophys. Res. Commun.* 69:538–547.

Eaton, W. A., and J. Hofrichter. 1987. Hemoglobin S gelation and sickle cell disease. *Blood.* 70:1245–1266.

Ferrone, F. A. 1989. Kinetic models and the pathophysiology of sickle cell disease. *Ann. NY Acad. Sci.* In press.

Ferrone, F. A., J. Hofrichter, H. Sunshine, and W. A. Eaton. 1980. Kinetic studies on photolysis-induced gelation of sickle cell hemoglobin suggest a new mechanism. *Biophys. J.* 32:361–377.

Ferrone, F. A., J. Hofrichter, and W. A. Eaton. 1985*a*. Kinetics of sickle hemoglobin polymerization I: studies using temperature-jump and laser photolysis techniques. *J. Mol. Biol.* 183:591–610.

Ferrone, F. A., J. Hofrichter, and W. A. Eaton. 1985*b*. Kinetics of sickle hemoglobin polymerization II: a double nucleation mechanism. *J. Mol. Biol.* 183:611–631.

Ferrone, F. A., M. R. Cho, and M. F. Bishop. 1986. Can a successful mechanism for hemoglobin S gelation predict sickle cell crises? *In* Approaches to the Therapy of Sickle Cell Anemia. INSERM, Paris) Y. Beuzard, S. Charache, and F. Galacteros, editors. 53–66.

Gerald, Curtis F. 1978. Applied Numerical Analysis. 2nd ed. Addison-Wesley Publishing Co., Reading, MA. 352 pp.

Herzfeld, I., and R. W. Briehl. 1981*a*. Phase behavior of reversibly polymerizing systems with narrow length distribution. *Macromolecules*. 14:397–404.

Herzfeld, J., and R. W. Briehl. 1981b. Length distributions and the alignment transition of polymers formed by linear reversible polymerization. *Macromolecules*. 14:1209–1214.

Hofrichter, J., P. D. Ross, and W. A. Eaton. 1974. Kinetics and mechanism of deoxyhemoglobin S gelation: a new approach to understanding sickle cell disease. *Proc. Natl. Acad. Sci. USA*. 71:4864–4868.

Hofrichter, J. 1975. An analysis of the birefringence intensity from gels of hemoglobin S. *J. Mol. Biol.* 96:254–256.

Hofrichter, J., P. D. Ross, and W. A. Eaton. 1976. A physical description of hemoglobin S gelation. *In* Proceedings of the Symposium on Molecular and Cellular Aspects of Sickle Cell Disease. J. I. Hercules, G. L. Cottam, M. R. Waterman, and A. N. Schechter, editors. Department of Health, Education and Welfare publication NIH 76-1007. 185–224.

Hofrichter, J. 1986. Kinetics of sickle hemoglobin polymerization III. Nucleation rates determined from stochastic fluctuations in polymerization progress curves. *J. Mol. Biol.* 189:553–571.

Kerker, M. 1969. The Scattering of Light and Other Electromagnetic Radiation. Academic Press, New York.

Mann, E. S. 1988. Length distributions of hemoglobin S fibers. *Biophys. J.* 53:282a. (Abstr.)

Mickols, W., M. F. Maestre, I. Tinoco, and S. H. Embury. 1985. Visualization of oriented hemoglobin S in individual erythrocytes by differential extinction of polarized light. *Proc. Nat. Acad. Sci. USA*. 82:6527–6531.

Mickols, W., J. D. Corbett, M. F. Maestre, I. Tinoco, J. Kropp, and S. H. Embury. 1988. The effect of speed of deoxygenation of the percentage of aligned hemoglobin in sickle cells. Application of differential polarization microscopy. *J. Biol. Chem.* 263:4338–4346.

Mozzarelli, A., J. Hofrichter, and W. A. Eaton. 1987. Delay time of hemoglobin S polymerization prevents most cells from sickling. *Science (Wash. DC)*. 237:500–506.

Oosawa, F., and S. Asakura. 1975. Thermodynamics of the Polymerization of Protein. Academic Press, New York. 51–53.

Ross, P. D., J. Hofrichter, and W. A. Eaton. 1975. Calorimetric and optical characterization of sickle cell hemoglobin gelation. *J. Mol. Biol.* 96:239–256.

Ross, P. D., J. Hofrichter, and W. A. Eaton. 1977. Thermodynamics of gelation of sickle cell deoxyhemoglobin. *J. Mol. Biol.* 115:111–134.

Sunshine, H. R., J. Hofrichter, W. A. Eaton. 1979. Gelation of sickle cell hemoglobin in mixtures with normal adult and fetal hemoglobins. *J. Mol. Biol.* 133:435–467.

Sunshine, H. R., J. Hofrichter, F. A. Ferrone, and W. A. Eaton. 1982. Oxygen binding by sickle cell hemoglobin polymers. *J. Mol. Biol.* 158:251–273.

van de Hulst, H. C. 1981. Light Scattering by Small Particles. Dover Publications, New York.

van Kampen, N. G. 1981. Stochastic Processes in Physics and Chemistry. North-Holland Publishing Co., Amsterdam. 139ff.

White, J. G., and B. Heagan. 1970. The fine structure of cell free sickled hemoglobin. *Am. J. Pathol.* 58:1–17.